# Triangular-Domain Basis Functions for Full-Wave Analysis of Microstrip Discontinuities

Robert Kipp and Chi H. Chan

*Abstract*—**A numerical technique for computing the S-parameters of arbitrarily shaped microstrip discontinuities and interconnects is presented. The microstrip conducing surface is rendered in a triangular discretization. Unknown currents are expanded with triangular-domain basis functions in a method of moments solution to the mixed-potential integral equation (MPIE). Triangular basis functions offer several advantages over rectangular subdomain functions, including their ability to conform readily to arbitrary geometries without "staircase" effect. Examples comparing triangular-domain modeling with rectangular-domain modeling and experiment are given.**

## I. Introduction

THE increasing switching speed and frequency of digital and analog circuits has expanded the need for characterizing board and chip-level microstrip interconnects without recourse to low-frequency or quasi-static approximations. The literature offers several full-wave approaches including mode matching [1], finite-difference time-domain FDTD [2], [3], and integral equation formulation solved with method of moments (MoM) [4], [5]. Some address specific geometries, such as microstrip step discontinuities [1] or open circuits and gaps [6], while others are intended for application to arbitrary configurations. In the latter category, the literature offers techniques based on MoM where the current on the upper conductor is expanded over rectangular subdomains in an approximate solution to the electric-field integral equation (EFIE) [7], [8] or mixed-potential integral equation (MPIE) [5]. This paper describes the application of triangular discretizations in the MoM solution of an MPIE formulation of scattering by microstrip interconnects and discontinuities.

Triangular subdomain basis functions were developed to compute scattering into a homogeneous medium by arbitrary surfaces [9]. Starting from an MPIE formulation, the unknown surface currents on a perfectly conducting object are obtained through MoM by rendering the surface in a nonuniform triangular mesh and expanding surface currents in basis functions defined over adjoining triangle pairs. More recently, this technique was extended to the inhomogeneous microstrip configuration to compute the surface current distribution and input impedances of microstrip patch antennas [10]. The efficient use of triangular basis functions in computing the S-parameters of microstrip discontinuities is detailed here.

Manuscript received May 14, 1992; revised November 2, 1992. This work was supported in part by the NSF, in part by the NSF(ECS-9158040) and NSF/Center for the design of Analog/Digital Integrated Circuits (CDADIC).

The authors are with the Department of Electrical Engineering, FT-10, University of Washington, Seattle, WA 98195.

IEEE Log Number 9209340.

Triangular discretization offers several advantages over rectangular discretization. The triangles conform exactly to any angled edges in the discontinuity, and curved edges are rendered in a line-segment rather than stair-case approximation. Transmission lines extending from the discontinuity at oblique angles are also represented without stair-case effect and handled with relative ease. Finally, triangular-domain functions offer greater flexibility in the use of nonuniform discretizations.

Section II provides a complete definition of the microstrip characterization problem considered here. The governing equation employed is the mixed-potential integral equation (MPIE) formulation, described in detail for microstrip in [11] and [12], and briefly repeated here for the sake of continuity. Section II also gives the equations for representing currents in triangular subdomains, and describes their incorporation into the MoM solution of the MPIE.

Specific implementation details for the microstrip S-parameter problem are given in Section III. The methodology is based on unimodal analysis of currents on the extended ports. In consequence, the ports are included in the scattering problem, and the number of unknowns often exceeds 1000. Hence, efficient solution requires efficient computation of the Green's functions within the MPIE. Evaluation of Green's function is accelerated with a technique developed in [13] and [14]; its important features are presented in Section III. One can also spare significant computational effort by identifying the redundant interactions among subdomain elements. These redundancies exist in abundance in the regions of the surface geometry where uniform discretization is viable. An approach for exploiting redundancy in arbitrary discretizations is described.

The MoM procedure renders the current distributions on the ports for a given excitation of the network. Scattering parameters can be extracted by computing the unimodal weighting coefficients for forward and reverse current waves on the ports. For an $N$-port discontinuity, no greater than $N$ linearly independent excitations are required, with structural symmetry reducing this number. A robust procedure for obtaining scattering parameters on an $N$-port is described in Section IV.

Numerical results are presented in Section V, with validation against experimental data for a microstrip stub and a coupled line. The results are also compared to those from a commercial microwave CAD package and, where possible, a full-wave, rectangular MoM code. Also considered is a 45° bend, whose $S_{11}$ reflection measurement and full-wave analysis with finite-difference time-domain (FDTD) method

are documented [3]. Finally, a comparison of the triangular and rectangular analyses of corner and miter bends is given. The corner bend can be exactly conformed by both rectangular and triangular discretization, while the miter bend can be exactly conformed only by the triangular discretization. Deficiencies in the rectangular approximation are identified.

## II. MPIE Formulation and Solution

### A. Problem Definition

The microstrip configuration considered here is illustrated in Fig. 1 and has arbitrary surface conductor geometry. The ground plane and substrate extend to infinity in the transverse direction, and the space above the dielectric is unbounded. The substrate is homogeneous and isotropic, but not necessarily lossless. The upper conductor and ground plane have zero resistivity, and the upper conductor is infinitely thin. The number of ports extending from the discontinuity is only limited by computation power. With some reformulation of the Green's functions, the procedure may be extended to include multiple dielectric and strip layers [12], [13].

With the goal of obtaining scattering parameters for a multiport discontinuity, the problem can be divided in two procedures: 1) obtain the surface current distribution on the discontinuity and extended ports under a number of excitation conditions; and 2) compute the scattering parameters from the currents on the ports.

### B. Computing Current Distribution

For a given excitation, the surface current distribution on the discontinuity and ports can be obtained by solving a relevant integral equation through the method of moments (MoM) [15]. We choose the mixed-potential integral equation (MPIE) over the electric-field integral equation (EFIE), as it has weaker singularities in its Green's functions, rendering more quickly convergent solutions [16].

The MPIE relates the electric-field incident upon the upper conductor to the magnetic vector and electric scalar potentials generated by the unknown surface current and charge densities [5]:

$$\boldsymbol{E}^{inc} = j\omega \boldsymbol{A} + \nabla \Phi \,, \tag{1}$$

where

$$\boldsymbol{A} = \int_S dS' \boldsymbol{J}(\boldsymbol{r}') G_a(\boldsymbol{r}, \boldsymbol{r}') \tag{2}$$

$$\Phi = \int_S dS' q_s G_q(\boldsymbol{r}, \boldsymbol{r}') \,. \tag{3}$$

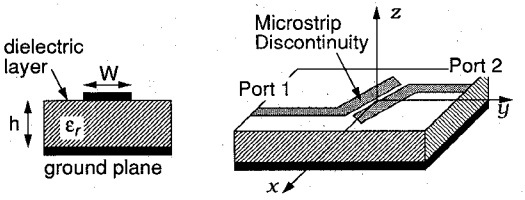


Fig. 1. Single layer microstrip geometry with a 2-port discontinuity.

The primed and unprimed coordinates, respectively, designate the source and field points. The Green's function $G_a$ is the horizontal component of the magnetic vector potential from an infinitesimal horizontal dipole located at the interface ($z' = 0$). $G_q$ is the electric scalar potential for a pulsating point-charge at the interface. Both potentials are evaluated at the interface, displaced from the source by radius $\rho$. $\boldsymbol{J}_s$ and $q_s$ are the surface current and surface charge densities on the upper microstrip conductor. The incident field $\boldsymbol{E}^{inc}$ provides the excitation to the system, the nature of which is addressed later in the discussion of S-parameter extraction.

As part of the MoM solution to (1), the unknown current and charge distributions are represented as a sum of vector basis functions weighted by unknown coefficients. Hence, current density $\boldsymbol{J}_s$ is approximated by

$$\boldsymbol{J}_s(\boldsymbol{r}) = \sum_{n=1}^{N} I_n \boldsymbol{f}_n \,. \tag{4}$$

Through application of the continuity condition

$$\nabla \cdot \boldsymbol{J}_s = -j\omega q_s \,, \tag{5}$$

the expansion of the charge distribution is obtained from (4), and no additional unknown coefficients are required.

Since the shape of the upper conductor is arbitrary, it is subdivided into small elements, with subdomain basis functions $\boldsymbol{f}_n$ approximating the current over each element. A possible discretization of a splitter is illustrated in Fig. 2. Here, we employ the triangular-domain basis functions developed in Rao *et al.* [9]. In this scheme, any two triangular plates sharing a side form a surface-current basis function, seen in Fig. 3. These functions overlap, and each plate can be part of up to three different basis functions. For any basis function $\boldsymbol{f}_n$, the two triangles are arbitrarily designated $T_n^+$ and $T_n^-$, with corresponding areas $A_n^+$ and $A_n^-$. The current dependence within $\boldsymbol{f}_n$ is given by

$$\boldsymbol{f}_n(\boldsymbol{r}) = \begin{cases} \frac{l_n}{2A_n^+} \boldsymbol{\rho}_n^+ & \text{if } \boldsymbol{r} \text{ in } T_n^+ \\ \frac{l_n}{2A_n^-} \boldsymbol{\rho}_n^- & \text{if } \boldsymbol{r} \text{ in } T_n^- \\ 0 & \text{otherwise} \end{cases} \tag{6}$$

where $l_n$ is the length of the common side and $\boldsymbol{\rho}_n^+ = \boldsymbol{r} - \boldsymbol{r}_n^+, \boldsymbol{\rho}_n^- = \boldsymbol{r}_n^- - \boldsymbol{r}$. A vector mapping of this dependence is given in Fig. 3. The current flows from plate $T_n^+$ to $T_n^-$, with maximum current across the common edge, zero current at the isolated vertices $V_n^+$ and $V_n^-$, and no currents with components

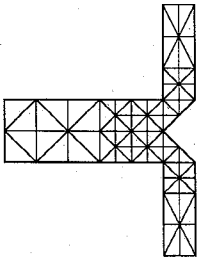

Fig. 2. Example of a triangular discretization for a splitter.

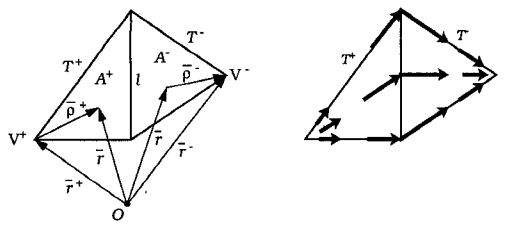


Fig. 3. Vector dependence of triangular-domain basis functions.

normal to the other four sides. The weighting in (6) is such that the current normal to the common edge is continuous across that edge and, hence, no fictitious charge singularities arise. Also, when the continuity equation is applied to (5), the charge density is a constant equal to $(l_n/A_n^+)$ and $-(l_n/A_n^-)$ on each plate and the total charge is zero.

The $N$ weighting coefficients in (4) are obtained through the Galerkin procedure whereby the $N$ basis functions are adopted as testing functions [9]. The result is the familiar MoM impedance matrix given by

$$\{V\} = [Z]\{I\} \tag{7}$$

where the $N$ rows in vector $V$ and matrix $Z$ correspond to the $N$ testing functions applied, respectively, to the left-hand side (LHS) and right-hand side (RHS) of (1), and the columns of matrix $Z$ represent the contribution of each basis function to the tested field. By solving this system of linear equations, the unknown weighting coefficients in vector $I$ are obtained. Defining the testing procedure in terms of the inner product operator

$$\langle a, b\rangle = \int_S dS\, a \cdot b\,, \tag{8}$$

we have

$$\langle \boldsymbol{E}^{inc}, \boldsymbol{f}_m\rangle = j\omega\langle \boldsymbol{A}, \boldsymbol{f}_m\rangle + \langle \nabla\Phi, \boldsymbol{f}_m\rangle \tag{9}$$

where $f_m(\boldsymbol{r})$ is the $m$th testing function. Evaluating (9) involves two surface integrals—one for the testing procedure and the other for the potentials within. The testing surface integral can be eliminated by assuming that potentials $\boldsymbol{A}$ and $\Phi$ and incident field $\boldsymbol{E}^{inc}$ within the domains of each triangle of $\boldsymbol{f}_m$ are constant and equal to their computed values at the triangle centroids. A further simplification is had by transferring the differential operator on $\Phi$ onto the testing function through integration by parts. Substituting (4) and (5) into (1), it can be shown that the elements of matrix $Z$ are given by

$$Z_{mn} = -l_m\left[j\omega\left(\boldsymbol{A}_{mn}^+ \cdot \frac{\rho_m^{c+}}{2} + \boldsymbol{A}_{mn}^- \cdot \frac{\rho_m^{c-}}{2}\right) + \Phi_{mn}^- - \Phi_{mn}^+\right] \tag{10}$$

where

$$\boldsymbol{A}_{mn}^{\pm} = \int_S dS'\, \boldsymbol{f}_n(\boldsymbol{r}')G_a\left(\boldsymbol{r}_m^{c\pm}, \boldsymbol{r}'\right) \tag{11}$$

$$\Phi_{mn}^{\pm} = \int_S dS'\, \nabla' \cdot \boldsymbol{f}_n(\boldsymbol{r}')G_q\left(\boldsymbol{r}_m^{c\pm}, \boldsymbol{r}'\right). \tag{12}$$

Here, $\rho_m^{c+}$ and $\rho_m^{c-}$ arise from evaluating testing function $\boldsymbol{f}_m$ at the centroids of $T_m^+$ and $T_m^-$. Observe in (12) that $\Delta \cdot \boldsymbol{f}_n$ is constant in each triangular domain and that, for a given basis/testing function pair $mn$, the contribution of the scalar potential in (10) depends upon the triangular plates involved but not the basis/testing function to which they are assigned. Hence, if the integral (12) is evaluated for each element $Z_{mn}$, many identical integrations will be performed. Considerable computational effort is saved by evaluating and storing (12) for all plate combinations and recalling these results as needed in evaluating (10).

The same cannot be said of (11), whose integrand evaluated over a particular source triangle depends on the identity of the isolated vertex and, hence, the basis function to which the triangle is assigned. However, a similar savings of effort is possible by breaking (11) into three scalar integrals

$$I_i = \int_S dS'\, g_i(\boldsymbol{r}')G_a\left(\boldsymbol{r}_m^{c\pm}, \boldsymbol{r}'\right) \tag{13}$$

where $g_i(\boldsymbol{r}')$ is set alternately to $x'$, $y'$, and 1. The basis function dependence is removed from the integrals and reintroduced in the evaluation of $Z_{mn}$ through a weighted sum of these three. Thus, for each plate combination, a total of four scalar integrals are evaluated and later recalled in constructing the elements in impedance matrix $Z$.

Finally, applying the approximate testing procedure in the LHS of (9), the elements of the excitation vector $V$ are given by

$$v_m = -l_m\left[\boldsymbol{E}^{inc}\left(\boldsymbol{r}_m^{c+}\right) \cdot \frac{\rho_m^{c+}}{2} + \boldsymbol{E}^{inc}\left(\boldsymbol{r}_m^{c-}\right) \cdot \frac{\rho_m^{c-}}{2}\right]. \tag{14}$$

Most of the elements $v_m$ will be zero, as the incident field is only applied in regions of port excitation, as discussed later.

## III. Efficient Implementation

### A. Efficient Evaluation of Green's Function

Generating the elements in matrix $Z$ with (10) requires convolution of the Green's functions $G_a$ and $G_q$ with the triangular basis functions, so it is necessary to evaluate them efficiently if acceptable solution times are to be achieved. There are no closed-form expressions for $G_a$ and $G_q$ in the spatial domain, but they can be represented in closed form in the spectral domain [14]

$$\tilde{G}_a = \frac{\mu_o}{4\pi}\frac{1}{j2k_{zo}}\left[1 + R_{TE}(k_\rho)\right] \tag{15}$$

$$\tilde{G}_q = \frac{1}{4\pi\epsilon_o}\frac{1}{j2k_{zo}}\left[1 + R_{TE} + \frac{k_{zo}^2}{k_\rho^2}\left(R_{TE} + R_{TM}\right)\right]. \tag{16}$$

Here, $\epsilon_o$ and $\mu_o$ are the free-space permittivity and permeability. Wave numbers $k_{zo}$ and $k_\rho$ are the vertical and radial components of the free-space propagation constant $k_o$ in the cylindrical system. $R_{TE}$ and $R_{TM}$ are the reflection coefficients at the interface of TE and TM plane waves incident on the substrate with ground plane. The required spatial-domain Green's functions can then be expressed as an

inverse Hankel transform on (15) and (16), which is commonly referred to as a Sommerfeld integral

$$G_{a,q}(\rho) = \int_{-\infty}^{+\infty} \tilde{G}_{a,q} H_0^{(2)}(k_\rho \rho) k_\rho \, dk_\rho \tag{17}$$

where $\rho$ is the radial separation between the source and the observation point, both located on the interface, and $H_0^{(2)}$ is the zeroth-order Hankel function of the second kind. The contour of integration can be deformed to avoid surface-wave poles, which reside on the real $k_\rho$ axis for lossless dielectrics and become complex for lossy dielectrics. Approximate analytic expressions exist for the evaluation of (17) for $\rho$ in the near and far fields [12], but intermediate regions require quadrature of slowly convergent, oscillatory integrands. However, a technique developed in [13] (and improved in [14]) allows efficient evaluation in all regions. The Sommerfeld integral is divided into three contributions: 1) quasi-dynamic images, 2) surface waves, and 3) complex images. The first two contributions, which dominate in the near and far field, respectively, are extracted from $R_{TE}$ and $R_{TM}$, and handled analytically using the Sommerfeld Identity [17]. What remains in $R_{TE}$ and $R_{TM}$ is relatively well behaved and exhibits exponential decay for sufficiently large values of $k_\rho$. This remainder can be accurately approximated with a short series of exponentials terms, which are interpreted as complex images. The function is sampled from $k_\rho = 0$ out to a truncation point where the exponential decay character dominates. The exponents of the expansion are computed using Prony's method [18], and the term weights are then obtained through a least-squares fit. The inverse Hankel transform of the exponentials can be performed analytically, again using the Sommerfeld Identity. Our experience indicates that 2–4 expansion terms are appropriate, depending on the frequency. Particular care should be taken in determining the number of expansion terms of $G_q$ since its contribution in (10) is a second-order difference arising from the source pulse doublet and the testing procedure. Overall, the process yields a reduction in computation time on the order of 100 compared to straight quadrature, and is essential in keeping the matrix fill time comparable to the matrix solve time. For this purpose, however, it is not sufficient; a means of exploiting redundant triangular interactions is also required.

### *B. Efficiencies of Discretization*

As explained in Section II, all elements in the impedance matrix can be computed from a linear combination of four scalar integrals evaluated for all source/test plate combinations. The number of these which must be computed can be significantly reduced by exploiting redundancy in the discretization and using approximate expressions when plates are separated by large distances. In the latter case, the surface integration over the source plate can be replaced by evaluation of the integrand at the plate centroid. Equations (11) and (12) become

$$\boldsymbol{A}_{mn}^{\pm} = \frac{l_n}{2}\left[\rho_n^{c+} G_a\left(\boldsymbol{r}_m^{\pm}, \boldsymbol{r}_n^{c+}\right) + \rho_n^{c-} G_a\left(\boldsymbol{r}_m^{\pm}, \boldsymbol{r}_n^{c-}\right)\right] \tag{18}$$

$$\Phi_{mn}^{\pm} = l_n\left[G_q\left(\boldsymbol{r}_m^{\pm}, \boldsymbol{r}_n^{c+}\right) - G_q\left(\boldsymbol{r}_m^{\pm}, \boldsymbol{r}_n^{c-}\right)\right]. \tag{19}$$

The criterion for distinguishing near and far interactions is based on the approximation used for the far interactions. If the percent difference between the distances from the three vertices of the source plate to the test plate centroid is under some set maximum level, say, 20%, then that approximation is viable. Since the great majority of plate interactions will often fall into the category of far interactions, it also makes sense to evaluate the Green's functions with an interpolation table, the construction of which is greatly expedited by the above described scheme for computing Green's functions. Both $G_a$ and $G_q$ exhibit $(1/\rho)$ and $\log \rho$ singularities, so the table must begin at some minimum displacement $\rho_0$ governed by the interpolation scheme, the dominant $(1/\rho)$ singularity, and a maximum error criterion, say, 1%. We use second-order differencing with an interval equal to 1% of the substrate wavelength and $\rho_0$ set to 3.5 times the interval.

For near interactions, approximations (18) and (19) cannot be used, and identification of redundancy is important to keeping the computational task manageable. The interactions can be cataloged by stepping through each plate combination. Far interactions are ignored, as they are too numerous to store and can be rapidly evaluated through the $G_a$ and $G_q$ interpolation tables at the point of computing the impedance $Z_{mn}$. For near interactions, the four scalar integrals from (12) and (13) are evaluated and cataloged. Subsequent plate combinations are then checked against the stored interactions and computed only if no equivalent interaction is available. Two plate interaction integrals are equivalent if the $x$- and $y$-displacements of the test plate centroid from the source plate vertices are identical. Here, too, significant improvements in efficiency are achieved by using, where possible, the interpolation tables in evaluating the integrals.

When all the efficiencies of discretization are combined with the method for rapid evaluation of the microstrip Green's functions and the elimination of the testing surface integral, the construction time for the impedance matrix is often comparable to, if not less than, the matrix solve time when the number of unknowns exceeds 500.

## IV. Extracting Scattering Parameters

Once the approximate current-density distribution is found by solving (7) for the unknown weighting coefficients, scattering parameters for an $N$-port discontinuity are obtained by examining the current distribution on the ports. In general, $N$ linearly independent excitation schemes are required to evaluate an $N$-port network, although physical symmetries in the discontinuity will reduce this. For example, a symmetric 2-port can be fully characterized by processing the current on both ports while excitation is provided to one port.

The ports are driven by applying horizontal voltage generators at the port ends. This is achieved by setting the incident electric field to some constant over the subcells at the port end(s). The corresponding elements $v_m$ in the excitation vector are assigned a nonzero quantity according to (14). While horizontal voltage sources are not the driving mechanism typically employed in practice, they are legitimately used here; the S-parameter extraction process only requires some form of

excitation which allows examination of a sufficient number of current samples on the ports between the discontinuity and the port ends. While the open-circuited port ends do affect the amplitudes of the current waves on the ports, the relationships among the waves incident upon and reflected from the discontinuity are nonetheless uniquely defined by its S-parameters [6].

With excitation applied, the sampled currents on the ports are fitted to the unimodal wave model

$$I_{ij}(x) = \frac{1}{\sqrt{Z_{oi}}}\left[a_{ij}e^{-\gamma_i x} - b_{ij}e^{+\gamma_i x}\right]. \tag{20}$$

Here we assume a port extending in the $x$-direction. $I_{ij}(x)$ is the sampled current distribution on the $i$th port for the $j$th excitation, obtained by integrating $J_x$ across the port width. If the port is discretized as shown in Fig. 4, we observe that only the highlighted basis functions have $x$-components at the indicated sample positions $x_n, x_{n+3}$. It can be shown from (5) that the current at one of these points is given by

$$I(x_n) = (i_1 + i_2)\Delta_y \tag{21}$$

where $i_1$ and $i_2$ are the weighting coefficients for the basis functions spanning the sample point. The uniform line characteristic impedance $Z_{0i}$ in (20), which can be obtained from a rigorous empirical formula [19], is necessary to normalize the currents when the ports are not identical. The propagation constant $\gamma_i$ is obtained by MoM analysis of a uniform line of the same dimensions at the port. Here, the current on an end driven uniform line is also fit to the form in (20) and $\gamma$ is optimized for smallest error in the fit. With these line constants known, forward and reverse complex wave coefficients $a$ and $b$ are generated through least-squares fit of the current samples to (20). In doing so, samples near the port end and discontinuity should be left out owing to the presence of decaying modes.

The S-parameters are obtained directly from the computed wave coefficients using the standard S-parameter matrix definition [20]. Recasting this matrix to solve for S-parameters, one finds, for example, that the $S_{11}$ and $S_{12}$ for an arbitrary 2-port are obtained by solving

$$\begin{bmatrix} a_1^1 & a_2^1 \\ a_1^2 & a_2^2 \end{bmatrix}\begin{bmatrix} S_{11} \\ S_{12} \end{bmatrix} = \begin{bmatrix} b_1^1 \\ b_1^2 \end{bmatrix} \tag{22}$$

where the subscripts on wave coefficients $a$ and $b$ denote the port, and the superscripts denote the excitation.

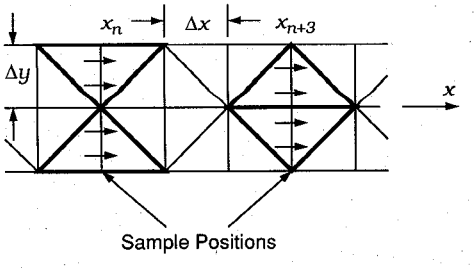


Fig. 4. Scheme for sampling the $x$-component of current on a uniform line.

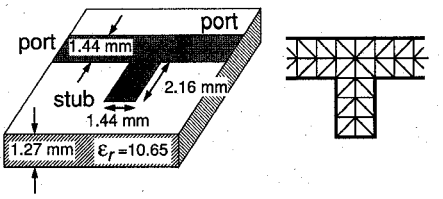


Fig. 5. Dimensions, substrate parameters, and discretization of microstrip stub.

## V. Numerical Results

### A. Validating Examples

In order to validate the above approach, including the approximations used to make it computationally tractable, several microstrip structures are simulated for which experimental data are available. The first of these is the microstrip stub whose geometry and discretization are given in Fig. 5. For the analysis using triangular MoM, the two ports extend 30 subcells each beyond those depicted in order to obtain a sufficient number of current samples. The bilateral symmetry in the stub is exploited in processing the port current data. A synopsis of the computational task in computing the current distribution for the stub and for the other cases which follow is provided in Table I. Itemized there are the typical CPU time (SPARC 2 workstation) per frequency point, matrix build/solve time ratio, number of unknowns (basis functions), number of triangular plates in the discretization, and the number of identified, unique plate-to-plate interactions; matrices were solved with LINPACK's complex, single-precision routine. The computed and measured responses are shown in Fig. 6; the measurement data are found in [8]. For comparison, also shown are responses generated by an MoM code using rectangular roof-top basis and razor-blade testing functions [21], and by Libra v. 3.000, the commercial microwave CAD package. The rectangular and the triangular MoM codes produce nearly identical results. Both predict the location of the measured stub resonance at 10.15 GHz to within 0.1 GHz, while the response generated by Libra shows resonance at 9 GHz. For Libra, the stub is constructed from a microstrip TEE circuit element attached to a section of open-circuited line with capacitive edge effect; these elements are operated within the specified regions of validity [22].

The second validation example is the coupled line whose geometry and discretization are seen in Fig. 7. The substrate parameters are $h = 1.524$ mm, $\varepsilon_r = 4.7$. The nonuniform discretization in the lateral direction of the couple-line pair is necessary to accurately account for the close coupling. The 45° bends at the ends of the lines are included to allow attachment of SMA connectors for measurements, conducted with a calibrated HP-8510B network analyzer and HP-8514A S-parameter test set. The measurement ends at 4 GHz due to limitations in the connectors. Results for $S_{21}$ and $S_{41}$ transmission coupling are given in Fig. 8(a) and (b). Simulation data are generated from the triangular MoM code and Libra. The 45° angle of the ports makes this structure cumbersome to model with rectangular basis functions, and no simulation is attempted with the rectangular MoM code. The

TABLE I
SYNOPSIS OF COMPUTATIONAL TASK FOR 3 DIFFERENT DISCONTINUITIES

| Device | CPU Time (min) | Build/Solve Time Ratio | Unknowns | Plates | Stored Interact. |
|---|---|---|---|---|---|
| Stub | 5.1 | 1.0 | 453 | 364 | 3210 |
| 45°-Bend (L) | 5.4 | 1.4 | 436 | 350 | 935 |
| 45°-Bend (H) | 75.2 | 0.5 | 1250 | 886 | 4247 |
| Coup. Line | 124.6 | 0.3 | 1536 | 1232 | 8692 |

test set contains two matched ports; the remaining two ports of the coupled line are terminated with match loads verified to produce less than -30 dB return over the measurement band. A separate measurement with a uniform line showed the SMA connectors to generate returns on the order of -25 to -15 dB in this measurement band. This precludes the possibility of a successful $S_{11}$ reflection measurement. For $S_{21}$ coupling, Libra and the MoM code are in good agreement with measurement up to 2.5 GHz, with the MoM code coming closer to predicting the magnitude of the band-pass peaks. Beyond 2.5 GHz, the measured coupling breaks out of its previous pattern. Both Libra and MoM fail to predict this, suggesting the emergence of nonideal phenomena in this frequency range, including increased reflection from the SMA connectors. For $S_{41}$ coupling, Libra and MoM are in close agreement, and both predict the overall character of the measurement. The gap between measurement and the computed response increases with frequency, again indicating the contributions of nonideal phenomena.

A third validation example is prompted by a recent paper presenting FDTD to simulate microstrip discontinuities [3]. The discontinuity is an unmitered 45° bend with line width $W = 2.4$ mm and substrate parameters $h = 0.79$ mm, $\varepsilon_r = 2.21$. The measured return loss in [3, Fig. 13] exhibits significant ringing—a result that cannot be explained by a single bend. The published FDTD results also show ringing, but they do not match well with experiment beyond 4 GHz. The simulation data using the TOUCHSTONE and TCKT commercial packages published in the same reference show a smooth increase in return loss with increasing frequency, and this agrees well with the trends predicted with our triangular MoM code under three different levels of discretization and simulation on Libra, seen in Fig. 9. Our Libra results identically match the published TOUCHSTONE results, which is to be expected, as Libra is an extension of TOUCHSTONE. We

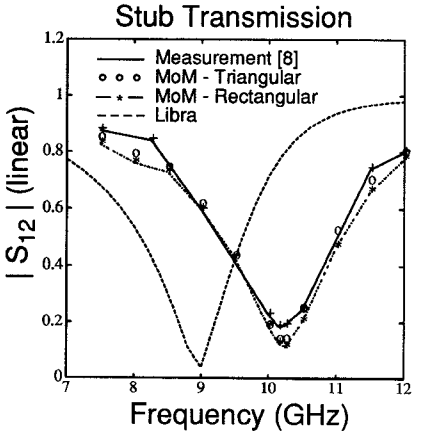


Fig. 6. Transmission response of stub; measured and computed with method-of-moments (triangular and rectangular basis functions) and Libra v 3.000.

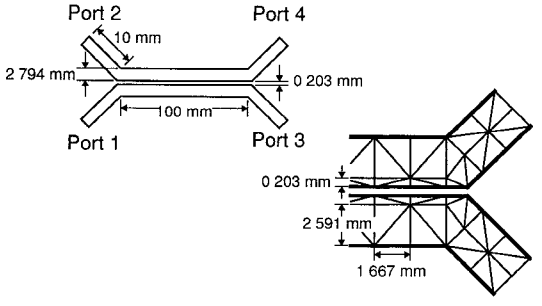


Fig. 7. Dimensions of coupled-line pair and a section of its discretization.

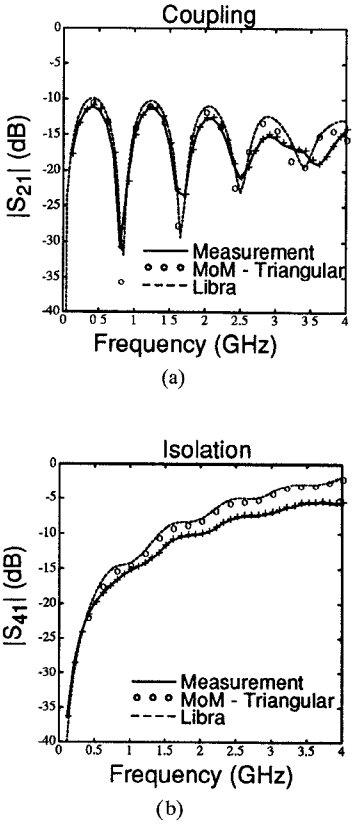


Fig. 8. Coupled-line transmission (a) $S_{21}$ and (b) $S_{41}$: measured and computed with triangular MoM and Libra v 3.000.

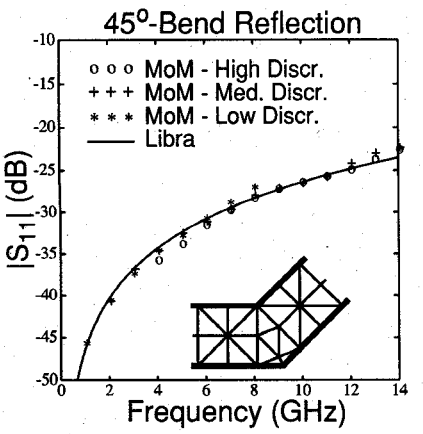


Fig. 9. Reflection response of 45°-bend computed with triangular MoM and Libra v 3.000.

believe that the measured ringing is induced by reflections at the ports, probably from connectors inadequate for this measurement. Judging from the return predicted by the Libra and TCKT packages and our MoM code, a connector with less than -45 dB return would be required for a good measurement. As mentioned earlier, our own experience using SMA coaxial-to-microstrip adaptors indicates that reflections below -20 dB cannot be reliably measured. Reference [3] does not indicate what manner of connection to the bend was used. It is our opinion that the ringing in the published FDTD response is probably due to the error introduced by the absorbing boundary condition [23].

For the MoM simulation, three different levels of discretization are used. There are 2, 4, and 6 square subcells spanning the line for the low, medium, and high levels of discretization; a portion of the low-level discretization is illustrated in Fig. 9. The two entries for the 45° bend in Table I are for the low and high discretization. All three give nearly identical results and agree with Libra in a frequency region where the reflections are all below -20 dB. No data are shown for the low discretization beyond 8 GHz, as it begins to fail at higher frequencies. Our experience indicates that there should be at least 20 subcells per wavelength to get acceptable results. This is a stiffer requirement than the 10-per-wavelength rule for MoM applied to far-field scattering problems; scattering parameters are more sensitive to errors in current than the far fields. At low frequencies, high levels of discretization are not only unnecessary but, in fact, become a liability as the electrical lengths of the ports shrink below one-quarter of a wavelength. While the port subcells can be stretched to maintain the electrical length of the port without increasing the number of unknowns, this introduces a discretization discontinuity whose effect, while small, can generate unacceptable errors in the computed reflection coefficient when the reflection from the actual discontinuity is also small, as is the case here. For this reason, the plotted results for the low, medium, and high discretizations begin at 1, 2, and 4 GHz, respectively.

### *B. Rectangular versus Triangular Discretization*

A microstrip corner bend and miter bend were simulated with the rectangular and triangular MoM codes to demonstrate

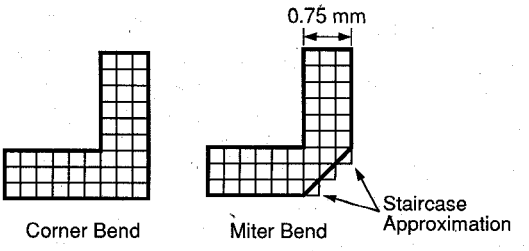


Fig. 10. Dimensions and discretization of corner and miter bends, with staircasing evident in rectangular discretization of miter bend.

the deficiencies which can arise from approximate representation of the conductor geometry. The geometry of the bends considered is described in Fig. 10; the ports, which extend 60 subdivisions, have been truncated for clarity. The substrate parameters are $h = 1.27$ mm, $\varepsilon_r = 10$. The corner bend can be exactly duplicated with either the triangular or rectangular discretization. The miter bend can be rendered exactly with the triangular discretization, but only approximately under a rectangular discretization. The staircase approximation of the miter bend was also conducted with the triangular MoM code. The computed $S_{11}$ reflections are shown in Fig. 11. The triangular and rectangular simulations of the corner bend and staircase approximated miter bend are in excellent agreement. The approximate miter bend has several decibels less reflection, as would be expected given a less abrupt transition. The true miter provides a still better transition, as evidenced by the simulation results under the triangular MoM code. The agreement between the triangular and rectangular code in the simulation of the corner and approximate miter bend shows that the predicted improvement in the true miter is due only to accurate rendering of the shape, and not to small numerical differences in two different computer codes.

## VI. Conclusion

A frequency-domain method for characterizing arbitrarily shaped, planar microstrip discontinuities has been described. This technique is based on solving the mixed-potential integral equation with the method of moments (MoM) under a triangular discretization of the microstrip upper conductor.

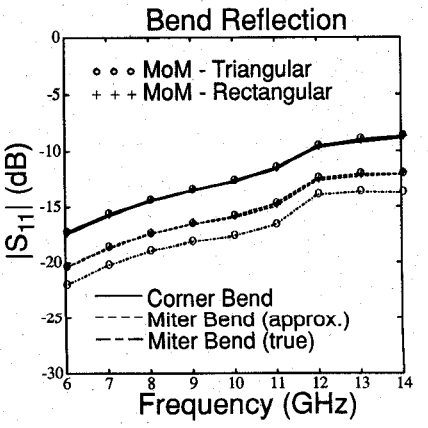


Fig. 11. Reflection response of corner bend and approximate miter bend computer with both triangular and rectangular MoM, and true miter bend computed with triangular MoM.

Triangular basis functions offer significant improvement over rectangular basis functions in their ability to conform to arbitrary shapes, including ports which extend at oblique angles. The implementation includes a number of techniques to significantly reduce the computational task including efficient evaluation of Green's function for microstrip and exploitation of redundancy in the discretization. These efficiencies allow simulations where the time spent filling the MoM impedance matrix is on the order of the time spent solving that matrix. Several validating examples confirm the overall approach. A study of a corner and miter bend shows how approximate rendering of a discontinuity in a rectangular discretization can degrade the accuracy of the simulation.

## ACKNOWLEDGMENT

We wish to acknowledge Dr. M. Soma and G. Devarayanadurg for providing the microstrip coupled-line device and for their assistance in measuring its S-parameters.

## REFERENCES

[1] T. S. Chu, T. Itoh, and Y.-C. Shih, "Comparative study of mode-matching formulations for microstrip discontinuity problems," *IEEE Trans. Microwave Theory Tech.*, vol. MTT-33, pp. 1018–1023, Oct. 1985.

[2] D. M. Sheen, S. M. Ali, M. D. Abouzahra, and J. A. Kong, "Application of the three-dimensional finite-difference time-domain method to the analysis of planar microstrip circuits," *IEEE Trans. Microwave Theory Tech.*, vol. 38, pp. 849–852, July 1990.

[3] J.-F. Lee, R. Palandech, and R. Mittra, "Modeling three-dimensional discontinuities in waveguides using nonorthogonal FDTD algorithm," *IEEE Trans. Microwave Theory Tech.*, vol. 40, pp. 346–352, Feb. 1992.

[4] R. W. Jackson and D. M. Pozar, "Full-wave analysis of microstrip open-end and gap discontinuities," *IEEE Trans. Microwave Theory Tech.*, vol. MTT-33, pp. 1036–1042, Oct. 1985.

[5] J. R. Mosig, "Arbitrarily shaped microstrip structures and their analysis with a mixed potential integral equation," *IEEE Trans. Microwave Theory Tech.*, vol. MTT-36, pp. 314–323, Feb. 1988.

[6] P. B. Katehi and N. G. Alexopoulos, "Frequency-dependent characteristics of microstrip discontinuities in millimeter-wave integrated circuits," *IEEE Trans. Microwave Theory Tech.*, vol. MTT-33, pp. 1029–1035, Oct. 1985.

[7] R. W. Jackson, "Full-wave finite element analysis of irregular microstrip discontinuities," *IEEE Trans. Microwave Theory Tech.*, vol. MTT-37, pp. 81–89, Jan. 1989.

[8] W. P. Harokopus and P. B. Katehi, "Characterization of microstrip discontinuities on multilayer dielectric substrates including radiation losses," *IEEE Trans. Microwave Theory Tech.*, vol. MTT-37, pp. 2058–2065, Dec. 1989.

[9] S. M. Rao, D. R. Wilton, and A. W. Glisson, "Electromagnetic scattering by surfaces of arbitrary shape," *IEEE Trans. Antennas Propogat.*, vol. AP-30, pp. 401–418, May 1982.

[10] K.-L. Wu, J. Litva, R. Fralich, and C. Wu, "Full wave analysis of arbitrarily shaped line-fed microstrip antennas using triangular finite-element method," *IEE Proc. H*, vol. 138, no. 5, pp. 421–428, Oct. 1991.

[11] J. R. Mosig and F. E. Gardiol, "Analytical and numerical techniques in the Green's function treatment of microstrip antennas and scatterers," *IEEE Proc. H*, vol. 130, no. 2, pp. 175–182, Mar. 1983.

[12] ——, "A dynamical radiation model for microstrip structures," in *Advances in Electronics and Electron Physic*, P. Hawkes, Ed. New York: Academic, 1982, pp. 139–237.

[13] D. G. Fang, J. J. Yang, and G. Y. Delisle, "Discrete image theory for horizontal electric dipoles in a multilayered medium above a conducting ground plane," *IEE Proc. H*, vol. 135, pp. 297–303, 1988.

[14] Y. L. Chow, J. J. Yang, D. G. Fang, and G. E. Howard, "A closed-form spatial Green's function for the thick microstrip substrate," *IEEE Trans. Microwave Theory Tech.*, vol. 39, pp. 588–592, Mar. 1991.

[15] R. F. Harrington, *Field Computation by Moment Methods.* New York: Macmillan, 1968.

[16] J. R. Mosig and F. E. Gardiol, "Integral equation techniques for the dynamic analysis of microstrip discontinuities," *Alta Frequenza*, vol. 57, no. 5, pp. 171–181, June 1988.

[17] A. Sommerfeld, *Partial Differential Equations.* New York: Academic, 1949.

[18] F. B. Hildebrand, *Introduction to Numerical Analysis.* New York: McGraw-Hill, 1974.

[19] I. Bahl and P. Bhartia, *Microwave Solid State Circuit Design.* New York: Wiley, 1988.

[20] R. F. Harrington, *Times-Harmonic Electromagnetic Fields.* New York: McGraw-Hill, 1961.

[21] R. Kipp, C. H. Chan, A. T. Yang, and J. T. Yao, "Simulation of high-frequency integrated circuits incorporating full-wave analysis of microstrip discontinuities," *IEEE Trans. Microwave Theory Tech.*, accepted for publication.

[22] *EEsof Element Catalog*, EEsof Inc., CA, 1989.

[23] J.-F. Lee, R. Palandech, and R. Mittra, "Corrections to "Modeling three-dimensional discontinuities in waveguides using nonorthogonal FDTD algorithm," *IEEE Trans. Microwave Theory Tech.*, vol. 40, pp. 1736, Aug. 1992.

**Robert Kipp** was born in Berwyn, IL, in 1965. He received the B.S.E.E. and B.S. degrees in mathematics from Rose-Hulman Institute of Technology, Terre Haute, IN, in 1987 and the M.S.E.E. degree from the University of Washington, Seattle, in 1990.

From July 1988 to December 1989, he was employed by the Boeing Co. as an Electromagnetics Engineer. He is presently pursuing the Ph.D. degree at the University of Washington, where we works in the Electromagnetics and Remote Sensing Laboratory as a Research Assistant. His research involves modeling of microstrip discontinuities and frequency selective surfaces.

**Chi H. Chan** attended Hong Kong Polytechnic and the City College of New York. He received the B.S. and M.S. degrees in electrical engineering from Ohio State University, Columbus, in 1981 and 1982, respectively, and the Ph.D. degree in electrical engineering from the University of Illinois, Urbana, in 1987.

From 1981 to 1982 he was a Graduate Research Associate at the ElectroScience Laboratory, Ohio State University. From 1987 to 1989 he was a Visiting Assistant Professor at the University of Illinois. In September 1989 he joined the University of Washington, Seattle, where he is currently an Associate Professor. His research interests include numerical techniques in electromagnetics, frequency-selective surfaces, microwave integrated circuits, high-speed digital circuits, wave propagation in anisotropic media for integrated optics applications, finite-element and finite-difference methods for remote sensing and biomedical applications, and neutral-networks techniques for inverse scattering and antenna designs. He has contributed to more than 80 journal and conference papers.

Dr. Chan is a member of URSI Commission B, and is a recipient of the 1991 NSF Presidential Young Investigator Award.